



**HAL**  
open science

## **Soils surrounding saline-alkaline lakes of Nhecolândia, Pantanal, Brazil: Toposequences, mineralogy and chemistry**

André Renan Costa-Silva, Yves Lucas, Ary Tavares Rezende-Filho, Mariana  
Dias Ramos, Patricia Merdy, Débora Ayumi Ishida, Laurent Barbiero,  
Adolpho José Melfi, Célia Regina Montes

### ► To cite this version:

André Renan Costa-Silva, Yves Lucas, Ary Tavares Rezende-Filho, Mariana Dias Ramos, Patricia Merdy, et al.. Soils surrounding saline-alkaline lakes of Nhecolândia, Pantanal, Brazil: Toposequences, mineralogy and chemistry. *Geoderma Régional*, 2024, 36, pp.e00746. 10.1016/j.geodrs.2023.e00746 . hal-04437294

**HAL Id: hal-04437294**

**<https://hal.science/hal-04437294>**

Submitted on 2 Apr 2024

**HAL** is a multi-disciplinary open access archive for the deposit and dissemination of scientific research documents, whether they are published or not. The documents may come from teaching and research institutions in France or abroad, or from public or private research centers.

L'archive ouverte pluridisciplinaire **HAL**, est destinée au dépôt et à la diffusion de documents scientifiques de niveau recherche, publiés ou non, émanant des établissements d'enseignement et de recherche français ou étrangers, des laboratoires publics ou privés.

1 **Soils surrounding saline-alkaline lakes of Nhecolândia,**  
2 **Pantanal, Brazil: toposequences, mineralogy and**  
3 **chemistry.**

4 André Renan Costa-Silva<sup>1,\*</sup>, Yves Lucas<sup>2</sup>, Ary Tavares  
5 Rezende Filho<sup>3</sup>, Mariana Dias Ramos<sup>4</sup>, Patricia Merdy<sup>2</sup>,  
6 Débora Ayumi Ishida<sup>5</sup>, Laurent Barbiero<sup>6</sup>, Adolpho José  
7 Melfi<sup>5</sup>, Célia Regina Montes<sup>1, 5</sup>

8 <sup>1</sup>CENA, LEST, Universidade de São Paulo, Piracicaba  
9 13400-970, Brasil.

10 <sup>2</sup>Université de Toulon, Aix Marseille Univ, CNRS,  
11 IM2NP, 83041 Toulon CEDEX 9, France.

12 <sup>3</sup>FAENG, Universidade Federal do Mato Grosso do  
13 Sul, Campo Grande 79079-000, Brasil

14 <sup>4</sup>IGCE, Universidade Estadual Paulista, Rio Claro  
15 13506-900, Brasil

16 <sup>5</sup>IEE, LEST, Universidade de São Paulo, São Paulo  
17 05508-010, Brasil.

18 <sup>6</sup>GET, IRD, CNRS, UPS, OMP, Toulouse 31400,  
19 France

20 \*Corresponding author.

Abbreviations: DOC: Dissolved organic carbon; DOM: Dissolved organic matter; EC<sub>S</sub>: Soil apparent electrical conductivity; EC<sub>W</sub>: Water electrical conductivity; EG: Ethylene glycol; ODFE: Oven-dried fine earth; OMF: Organic matter free.

21 E-mail address: andrerenan00@usp.br (A. R. Costa-  
22 Silva).

23 Postal address: Centro de Energia Nuclear na  
24 Agricultura (CENA), Universidade de São Paulo, Av.  
25 Centenário, 303, São Dimas, 13416-000, Piracicaba, São  
26 Paulo, Brasil.

27 Contact numbers: +5585981828161 or  
28 +330615278748

## 29 **ABSTRACT**

30 The Nhecolândia subregion of the Brazilian Pantanal is a  
31 vast fluviolacustrine system subject to a very seasonal  
32 climate, which is distinguished by freshwater or saline-  
33 alkaline lakes of different types: green due to cyanobacterial  
34 bloom, black due to dissolved organic matter, or crystalline.  
35 Numerous studies carried out in the region over the past  
36 twenty years on the lakes and the surrounding soils have  
37 shown probable relationships between the saline-alkaline  
38 character of the lakes, the surrounding soils and the  
39 dynamics of the water tables. These results, however, have  
40 been acquired by independent studies on many different  
41 sites, which makes their synthesis difficult, and they leave

42 open the question of the causes of the difference between  
43 lake types. Here we have begun to study on a single site  
44 representative of the Nhecolândia area, all the factors  
45 thought to be necessary to understand the genesis and  
46 dynamics of the soils and lakes. For each type of lake, we  
47 carried out detailed toposequence soil studies and  
48 characterized the granulometry, chemistry and mineralogy of  
49 the identified horizons. A 45-month temporal study of  
50 satellite data was used to assess the connection of the lakes  
51 to the seasonal flood network. Our results confirmed the  
52 general organization and mineralogy of the soil covers  
53 around saline-alkaline lakes. We have determined the  
54 differences between the soil toposequences corresponding  
55 to the slopes of the different types of lakes. We have found  
56 that two types of silcrete can be formed, one being acidic  
57 and the other alkaline. We have shown that, among the  
58 conditions which guarantee endorheism, which leads to the  
59 alkalization of lakes, the presence of a ridge around a lake  
60 is not sufficient, but that the presence of deep impermeable  
61 horizons in the lower half of the toposequences is  
62 necessary. Crystalline lakes could differentiate from black  
63 and green ones due to less efficient hydraulic isolation. We

64 provide a large data set relative to a single site which will  
65 help guide and develop more specific studies on these  
66 alkaline systems.

67 **Keywords:** Pantanal, Nhecolândia, Arenosols, Solonetz,  
68 Silcrete, Petroduric horizon.

## 69 1. INTRODUCTION

70 The Pantanal subregion of Nhecolândia is a large  
71 lacustrine system developed on sandy sediments deposited  
72 from the Pleistocene to the Upper Holocene. The lakes are  
73 formed by the partial obstruction of river beds by small  
74 forested ridges, locally known as *cordilheiras*, in the distal  
75 portion of distributary lobes of the Taquari river sedimentary  
76 megafan (Assine et al., 2015). With more than 10,000 lakes,  
77 which are mostly shallow and ranging from 0.025 to 0.15 km<sup>2</sup>  
78 (Costa et al., 2015; Pereira et al., 2020). The lacustrine  
79 system is dominated by freshwater lakes, known locally as  
80 *baías*, but around 7% are saline-alkaline lakes or *salinas*,  
81 surrounded by alkaline soils (Almeida, 2007; Furian et al.,  
82 2013). Saline-alkaline lakes can still be subdivided according  
83 to the color of their waters which varies between green, due  
84 to the proliferation of cyanobacteria, black, due to high

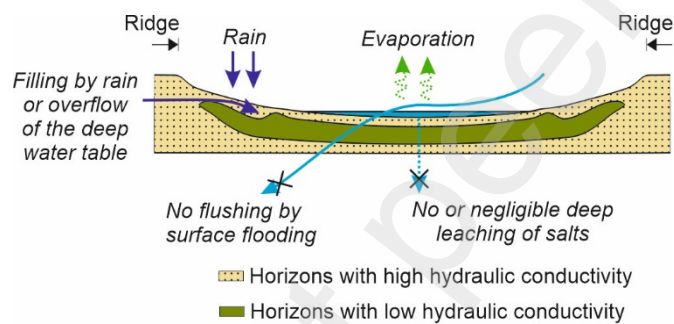
85 concentrations of dissolved organic matter (DOM) and  
86 crystalline (Barbiero et al., 2008; Curti-Martins, 2012, Cotta  
87 et al, 2022; Pellegrinetti et al, 2022).

88           The Pantanal is a low-lying region with a semi-humid  
89 tropical climate characterized by dry winter and rainy  
90 summer, controlled mainly by the South American monsoon  
91 (Zhou and Lau, 1998; Sakamoto et al., 2004; Furquim et al.,  
92 2008; Furian et al., 2013). The interaction between the  
93 regional rainfall pattern, the stock and the discharge of  
94 groundwater generates an annual evapotranspiration rate  
95 greater than that of precipitation (Hamilton et al., 1998; Alho,  
96 2008; Guerreiro, 2016). Despite the negative annual water  
97 balance, precipitation in the rainy season is sufficient to  
98 leach the soluble species accumulated in the soil by  
99 evaporation in the dry season (Hamilton et al., 1998; INMET,  
100 2020). The present-day rainfall regime does not explain the  
101 presence of alkaline soils and therefore, other processes  
102 must be considered.

103           Numerous studies carried out in the region over the  
104 past twenty years have ruled out the hypothesis that salinity  
105 is inherited from drier periods of the past, demonstrating that  
106 the saline-alkaline lakes are very probably isolated from the

107 surface drainage network. This disconnection would result in  
108 an endorheic-type system (Fig. 1): during the rainy season,  
109 saline-alkaline lakes are not flooded but only recharged by  
110 rainfall or lateral flow of groundwater; during the dry season,  
111 evaporation from the surface of the lake and by capillary rise  
112 from the surrounding soils concentrates the soluble species  
113 (Barbiero et al., 2002, 2008; Almeida et al., 2007; Furian et  
114 al., 2013). Some authors consider that lateral flow of fresh  
115 groundwater between lakes may continue during the dry  
116 season. The soils surrounding these lakes become alkaline,  
117 which results in values of soil electrical conductivity (ECs),  
118 pH and dissolved organic carbon (DOC) in soil water  
119 reaching  $80 \text{ dS.m}^{-1}$ , 11 and  $750 \text{ mgC.L}^{-1}$ , respectively  
120 (Mariot et al., 2007; Barbiero et al., 2008). They exhibit a  
121 number of characteristic features, in particular, the presence  
122 of deep, low-permeability green horizons, which are the sites  
123 of neoformation of specific secondary clay minerals,  
124 stevensite or Fe-illite (Barbiero et al., 2008; Furquim et al.,  
125 2008, 2010a, 2010b; Furian et al., 2013; Andrade et al.,  
126 2020; Vidoca et al., 2020; Souza Oliveira et al., 2021). The  
127 3-D morphology of the green horizons may govern part of  
128 the lake groundwater dynamics (Sakamoto et al., 2004;

129 Barbiero et al., 2008; Furian et al., 2013; Freitas et al.,  
 130 2019). Recent geochemical modeling has shown that 125  
 131 years of endorheic functioning are sufficient to reach the  
 132 observed alkalinities (Merdy et al., 2022). These last authors  
 133 noted that the alkaline character of the lakes and soils can  
 134 disappear if new drainage conditions allow an export of the  
 135 labile elements out of the system.



136  
 137 *Fig. 1. Water dynamics - Main routes of water transfer in an alkaline lake*  
 138 *according to the literature. (For colour the reader is referred to the web*  
 139 *version of this article)*

140 The results and interpretations presented above  
 141 leave a few questions remaining. Firstly, the disconnection  
 142 between saline-alkaline lakes and the surface drainage  
 143 network, although very probable, has never been formally  
 144 demonstrated by a long-term study. Another uncertainty is  
 145 how does the alkalization process begin, particularly the



146 waterproofing of green horizons? Finally, how is the saline-  
147 alkaline lake type determined?

148           With this in mind, this study aims to characterize the  
149 soil dynamics of a representative site under various factors  
150 that may influence the geochemistry of saline-alkaline lakes.  
151 The disconnection of the selected environments from  
152 superficial drainage during different seasons, despite the  
153 proximity of ephemeral recharge channels, suggests that the  
154 soil, and more particularly its mineralogy, can act as  
155 determinant factors for those types of environments and their  
156 differences.

## 157 **2. MATERIAL AND METHODS**

### 158 **2.1. Lake selection**

159           Studied soils are located inside the Fazenda São  
160 Roque (19°23'26" S and 56°19'33" W), in the municipality of  
161 Aquidauana (Mato Grosso do Sul, Brazil) (Fig. 2). Four  
162 saline-alkaline lakes were selected as representatives of the  
163 southern subregion of the of Nhecolândia lacustrine system  
164 following the testing of electric conductivity ( $EC_w$ ), pH,  $E_H$   
165 and turbidity of each lake water (Table 1): one crystal-clear  
166 water lake (7-Crystalline), two black water lakes (1-Black

167 and 6-Black) and one green water lake (4-Green) (Fig. 2).

168 Five freshwater lakes were also considered for spatial

169 analysis.

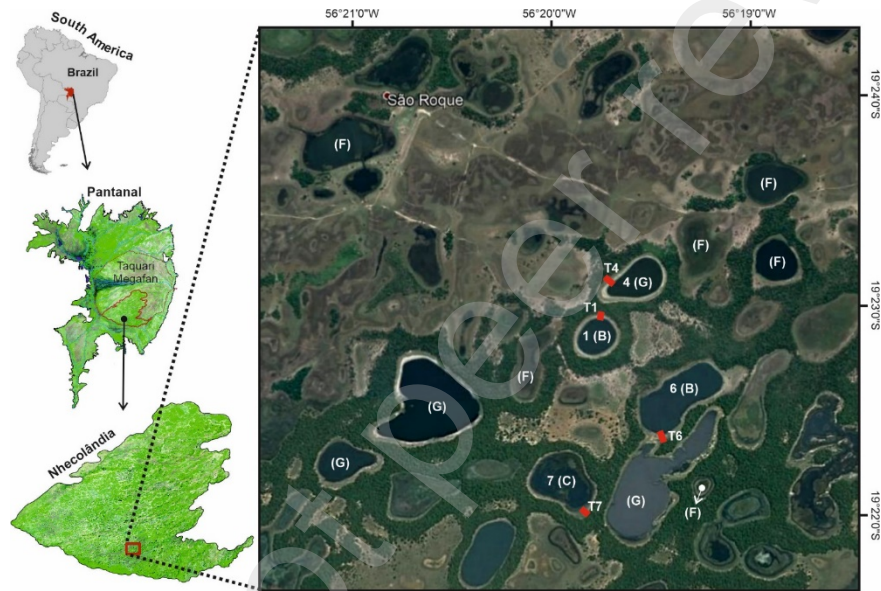
170 *Table 1. Saline-alkaline lake data*

171 *Parameters used to select representative saline-alkaline lakes within the*

172 *study site.*

	<b>1-Black</b>	<b>4-Green</b>	<b>6-Black</b>	<b>7-Crystalline</b>
<i>Water Electrical</i>	3500 (Jul/17)	3420 (Jul/17)	1662 (Jul/17)	826 (Sep/19)
<i>Conductivity</i>	3340 (Jul/17)	8730 (Sep/17)	28240 (oct/17)	
<i>(EC<sub>w</sub> - <math>\mu\text{Scm}^{-1}</math>)</i>	8160 (Sep/17)	2990 (Sep/19)	1490 (Sep/19)	
	2270 (Sep/19)	3950 (Sep/19)	2050 (oct/19)	
		4990 (Sep/19)		
		5750 (oct/19)		
<i>Water</i>	31 (Jul/17)	27,4 (Jul/17)	26,6 (Jul/17)	25,5 (Sep/19)
<i>temperature (°C)</i>	24,5 (Jul/17)	26,3 (Sep/19)	24,8 (Sep/19)	
<i>Water pH</i>	9,67 (Jul/17)	10,30 (Jul/17)	9,45 (Jul/17)	8,62 (Sep/19)
	9,70 (Jul/17)	9,76 (Sep/19)	9,24 (Sep/19)	
	9,35 (Sep/19)			
<i>Water redox</i>	+93,8 (Jul/17)	+88,9 (Jul/17)	+207,2 (Jul/17)	+50,0 (Sep/19)
<i>potencial (mV)</i>	+90,6 (Jul/17)	+88,7 (Jul/17)	+201,4 (Jul/17)	
	+88,3 (Jul/17)	-30,0 (Sep/19)	+192,1 (Jul/17)	
	-15,0 (Sep/19)		+90,0 (Sep/19)	
<i>Sediment redox</i>	-399,3 (Jul/17)	-408,5 (Jul/17)	-3,4 (Jul/17)	-280,0 (Sep/19)
<i>potencial (mV)</i>	-536,9 (Jul/17)	-418,3 (Jul/17)	-3,0 (Jul/17)	
		-430,0 (Sep/19)		

	-541,3 (Jul/17)		-9,7 (Jul/17)	
	-450,0 (Sep/19)		-220,0 (Sep/19)	
<i>Turbidity (NTU)</i>	28 (Jul/17)	>1000 (Jul/17)	117 (Jul/17)	1,8 (Sep/19)
	75 (Sep/19)	466 (Sep/19)	108 (Sep/19)	



173

174 *Fig. 2. Location of study - Sites in the Nhecolândia area of the Taquari*  
 175 *megafan, Pantanal, Brazil. Saline-alkaline lakes (1, 4, 6, 7) (B: black, G:*  
 176 *green; C: crystalline) and freshwater lakes (F). T1 to T7: toposequences*  
 177 *associated to the studied lakes. Satellite view from Google Earth. (For*  
 178 *colour the reader is referred to the web version of this article)*

## 179 **2.2. Spatial data**

180 Fluviometric data relied on the processing of 102  
 181 PlanetScope images on Google Earth Engine and ArcGIS  
 182 10.5 platforms, using supervised classifiers (Random Forest)

183 in a 45-month time series. The sensor system absorbs the  
184 reflectance of targets in the visible light spectrum, as well as  
185 in the blue (455-515 nm), green (500-590 nm) and red (590-  
186 670 nm) bands, in addition to near infrared (780-860 nm),  
187 resulting in 16-bit images of radiometric information  
188 (PLANET LABS, 2016). Orthorectified and atmospheric  
189 corrected (absence of clouds) 7x25 km images with a spatial  
190 resolution of 3 meters and with a passing time between 9:30  
191 am and 11:30 am UTC, were selected fortnightly between  
192 October 2017 and July 2021. The study aimed to verify the  
193 disconnection of the studied saline-alkaline lakes from the  
194 surface drainage network. A quantitative value of 1 was  
195 assigned to pixels linked with the presence of water, the  
196 value of 0.5 for pixels associated with areas subject to  
197 seasonal flooding, and a 0 value for permanently dry areas.  
198 The flood frequency map was then obtained from a reducer  
199 ('*reduce.sum*') applied over the entire image collection.  
200 Google Earth Engine reducers allowed the acquisition of  
201 statistical and arithmetic data as they operate across the  
202 stack of images that make up the time series (GOOGLE,  
203 2020).

### 204 **2.3. Field work**

205           The soil characterization was carried out along  
206 toposequences, following the Boulet et al. (1982) method.  
207 The toposequences were positioned on the lake slopes in  
208 regions of greater EC contrasts measured from the surface  
209 with an EM38 electromagnetic conductivity meter (Geonics  
210 Ltd, Canada), with the aim of observing the widest range of  
211 soil variations. Microforms of local relief, lake levels and  
212 drilling positions were obtained with greater than centimeter  
213 precision from topographic data collected using the Global  
214 Navigation Satellite System with Real-Time Kinematic  
215 (GNSS-RTK) positioning. Soil macromorphological  
216 characteristics were collected in boreholes drilled by manual  
217 auger and cased to prevent collapsing. Soil colors were  
218 obtained following Munsell (1954) references. When  
219 possible, the depth, pH and  $CE_w$  of the water tables were  
220 measured at the drilling time and 24 h after.

### 221 **2.4. Laboratory procedures**

222           Soil samples were dried in a ventilated drying oven  
223 at 40° C, crushed and sieved with a 2-mm mesh to obtain  
224 oven-dried fine earth (ODFE). When necessary, samples

225 were ground and sieved with a 150 mesh (106  $\mu\text{m}$ ) and/or  
226 organic matter was removed with sodium hypochlorite  
227 ( $\text{NaClO}$ ) at pH 9.5 (Anderson, 1963), resulting in powder and  
228 organic matter free (OMF) aliquots. Particle size distribution  
229 was determined by the Robinson pipette method (Pansu and  
230 Gautheyrou, 2006) and textural classes were denominated  
231 according to the USDA (1987). Clay and silt fractions were  
232 obtained by centrifugation (Jackson, 1985). It should be  
233 noted that the mode of separation of the clay fraction, which  
234 requires suspension in ultrapure water, is likely to dissolve  
235 minerals such as evaporitic minerals or very small  
236 carbonates. Soil pH was measured from the ODFE with a  
237 1:2.5 w:w soil:water ratio (EMBRAPA, 2017). Total chemical  
238 analysis for major element determinations was performed  
239 using total melting of soil samples and measured by  
240 Inductively Coupled Plasma Optical Emission Spectroscopy  
241 (ICP-OES).

## 242 **2.5. Mineralogical analysis**

243 Most soil minerals were characterized by X-ray  
244 Diffractometry (XRD) and Fourier Transform Infrared  
245 spectroscopy (FTIR). Diffuse Reflectance Spectroscopy

246 (DRS) was used for the identification of iron oxides and oxy-  
247 hydroxides. XRD samples were analyzed using a Philips PW  
248 1877 diffractometer (Philips, Amsterdam, Netherlands)  
249 operated at 40kV potential, 40mA current, using  $\text{CuK}\alpha$   
250 radiation with a graphite crystal monochromator. The scan  
251 was performed from  $3^\circ$  to  $90^\circ$  ( $2\theta$ ) with a step of  $0.02^\circ$  and  
252 2,5 seconds per time accumulation step. Mineral phases  
253 were identified on the X' Pert HighScore Plus version 4.9  
254 software (Malvern Panalytical, Netherlands). XRD analysis  
255 was performed on the clay fraction ( $<2 \mu\text{m}$ ) from the ODFE  
256 and OMF aliquots, oriented and saturated (1) with  
257 magnesium chloride ( $\text{MgCl}_2$ ), later solvated with ethylene  
258 glycol (EG), and (2) with potassium chloride (KCl), later  
259 heated to 110 and 550  $^\circ\text{C}$  (Wilson, 1987).

260 Representative peaks used for mineral identification  
261 were the following: quartz, 3.34Å, 4.25Å and 1.81Å;  
262 feldspars (microcline and/or orthoclase), 3.24Å, 4.21Å and  
263 3.29Å; micas (muscovite and/or illite), 4.29Å, 3.86Å and  
264 10Å; kaolinite, 7.13Å, 3.56Å and 4.35Å; 2:1 expandable clay  
265 minerals (montmorillonite and/or vermiculite), 12 to 15Å;  
266 calcite, 3.02Å, 1.87Å and 2.28Å.

267 FTIR was performed on OMF clay mixed with  
268 potassium bromide (KBr) pellets prepared with KBr Tablet  
269 Die using a Shimadzu IR Prestige-21 spectrophotometer  
270 (Shimadzu, Japan), with spectra from 400 to 4600 cm<sup>-1</sup>.  
271 Saturation or low-resolution bands were re-evaluated in  
272 replicates with lower or higher sample mass pellets.  
273 Normalization of results was achieved by the mineral phase  
274 band with the highest absorption, considering an absorbance  
275 correction factor based on mass values of sample, KBr and  
276 pellets. The identification of mineral phases was performed  
277 by characteristic absorption bands (Russel and Fraser,  
278 1994; Ekosse, 2005; Vaculíková and Plevová, 2005; Saikia  
279 et al., 2008; Ji et al., 2009; Theodosoglou et al. 2010; Lainé  
280 et al., 2017; Acevedo et al., 2017; Zviagina et al., 2020).

281 The identification of iron oxides and oxy-hydroxides  
282 by DRS was performed on powder ODFE and OMF clay in a  
283 Cary 5 spectrometer (UV-VIS-NIR) (Varian, USA). The  
284 samples were analyzed in triplicate, ranging from 370 to  
285 820nm with increments of 0.1nm. The reflectance R was  
286 measured in comparison to a Halon pattern and transformed  
287 into the Kubelka-Munk remission function  $[f(R) = (1 - R)^2 / 2$   
288  $R]$ . From the obtained curves, the second derivative was



289 calculated and mineral phases were identified through  
290 characteristic absorption bands  ${}^4E:4A_i$  and EPT (Electronic  
291 Pair Transition) (Kosmas, 1984; Malengreau et al., 1996;  
292 Scheinost et al., 1998; Cornell and Schwertmann, 2000).  
293 Identification of goethite and hematite was made by  
294 comparison with characteristic absorption bands in  
295 commercial standards (Sigma-Aldrich 71063 and 310050,  
296 respectively).

## 297 **2.6. Statistics**

298 Principal components analysis (PCA) was performed  
299 using XLSTAT 2017 on various sets of the obtained data.  
300 PCA project multidimensional data clouds to subspace in  
301 order to minimize the residual variance, choosing the most  
302 relevant directions (principal components) in the data (Jolliffe  
303 2002). We chose a correlation based PCA on standardized  
304 variables to avoid sensitivity to the scaling of the variables.

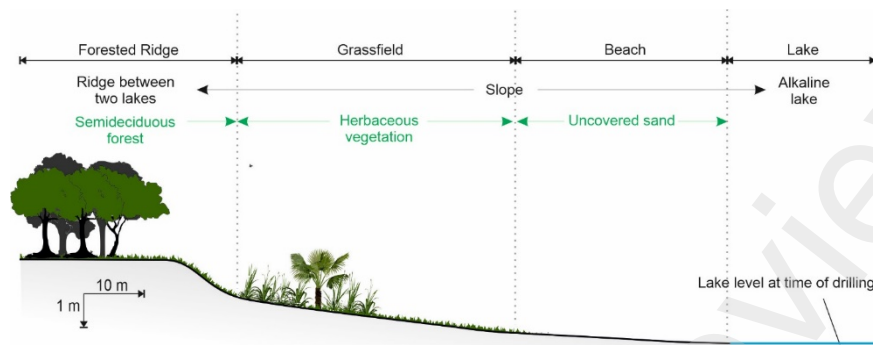
## 305 **3. RESULTS AND DISCUSSION**

### 306 **3.1. Study site and lake characteristics**

307 The fieldwork was carried out at the end of the dry  
308 season, which is the time of year when motorized land  
309 access to the study site is possible, in October 2017,

310 September 2018, October 2019 and November 2020. During  
311 collection of soil samples, physicochemical parameters of  
312 waters and sediments from within the selected saline-  
313 alkaline lakes (Fig. 1) were monitored and are presented in  
314 Table 1. The crystalline-type lake and the green-type lake  
315 had the lowest and highest pH and turbidity values,  
316 respectively, the black-type lakes being in between.  
317 Significant  $EC_w$  variations were observed according to time  
318 period, ranging from 826  $\mu\text{S}/\text{cm}$  (7-Crystalline lake on  
319 September 2019) to 28240  $\mu\text{S}/\text{cm}$  (6-Black lake on October  
320 2017).

321 The alkaline lakes showed a typical succession of  
322 vegetation from their upper part to their lower part: *cerrado*  
323 type savanna forest on the sandy ridges and a succession of  
324 savanna woodland, open woody savanna, open shrubby  
325 grassfield with palm trees and savanna grassfield on the  
326 slopes, susceptible to differentiation by the predominance of  
327 *andropogon bicorns* (*capim-de-burro*) and *cynodon dactylon*  
328 grass species (Salis et al., 2014) (Fig. 3).



329

330 *Fig. 3. Landscape units - Typical vegetation along a saline-alkaline lake*331 *slope.*

332 The lake biota differed between lake types

333 (Pellegrinetti et al., 2022). It was oligotrophic vegetated for

334 the 7-Crystalline lake, oligotrophic turbid for the 1-Black and

335 6-Black lakes, and eutrophic for the 4-Green lake

336 **3.2. Spatial Analysis**

337 The 102 PlanetScope satellite images showed that

338 the four studied saline-alkaline lakes are all surrounded by

339 forested sandy ridges, the altitude of which is more than 2 m

340 higher than the surface of the lakes at the end of the wet

341 season (Fig. 4). Although all taken in the same season, the

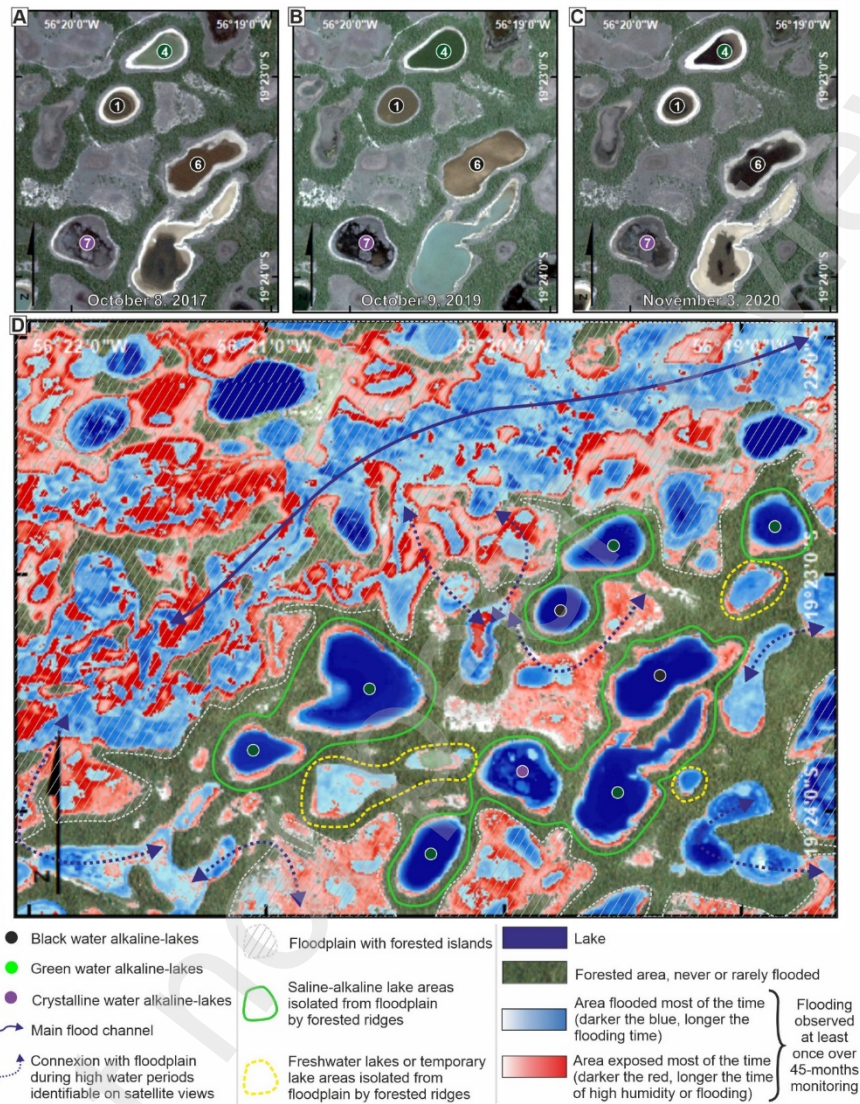
342 views show significant variations in the levels of the lakes,

343 resulting from the rainfall of previous months. In October

344 2019 (Fig. 4B), the lakes had a rather high water level for the

345 end of the dry season due to regular rainfall in the previous

346 rainy season. In November 2020 (Fig. 4C), the lakes had  
347 very low water levels, with some almost dry, due to low  
348 rainfall in the previous rainy season. The situation was  
349 intermediate in October 2017 (Fig. 4A). These observations  
350 underline the strong interannual heterogeneity of  
351 precipitation.



352

353 *Fig. 4. Flooding monitoring - Interannual variability of the water level in*  
 354 *the lakes studied. Satellite views from PlanetScope. (For colour the*  
 355 *reader is referred to the web version of this article).*

356

357

358

The flooding dynamics in the area are outlined in

Fig. 4D. Patches of lighter blue tones inside the 7-Crystalline

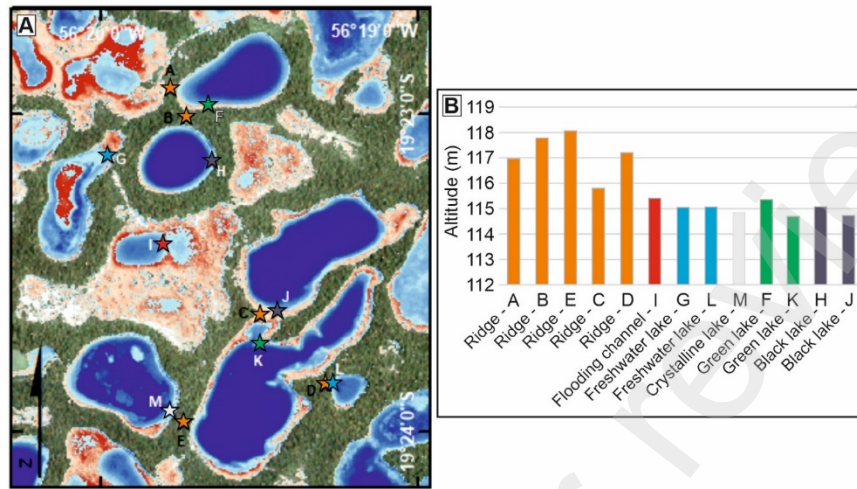
lake are due to the presence of macrophytes and their

359 spectral reflectance characteristics. The ephemeral flood  
360 channels, regionally called *vazantes*, follow the  
361 geomorphological description of Cunha (1980) of smooth  
362 and elongated depressions that distribute the incoming  
363 floods, thus corresponding to periodically flooded soils. The  
364 main flood channel of the area (called *Mangabal vazante*) is  
365 connected with the Taquari River and responsible for the  
366 terrestrial surface recharge of freshwater lakes during the  
367 rainy season (plain line arrow; Fig. 4). For most freshwater  
368 lakes located outside the floodplain, it is possible to identify  
369 temporarily active connections with the floodplain (dotted  
370 arrows; Fig. 4). Some freshwater lakes, however, are  
371 surrounded by forested ridges with no identifiable connection  
372 to floodplains. As for the hypothesis to which the saline-  
373 alkaline lakes would result from a disconnection with the  
374 superficial hydrographic network, this shows that the mere  
375 presence of a forested ridge is insufficient to ensure such a  
376 disconnection.

377           Levels of saline-alkaline and freshwater lakes  
378 measured during the same day in November 2019 are given  
379 in Fig. 5B. The same elevation of freshwater lakes could  
380 indicate a regional water table level; the different elevation of

381 the alkaline lakes could indicate a hydraulic disconnection of  
382 these lakes with regional groundwater (Fig. 5).

Preprint not peer reviewed



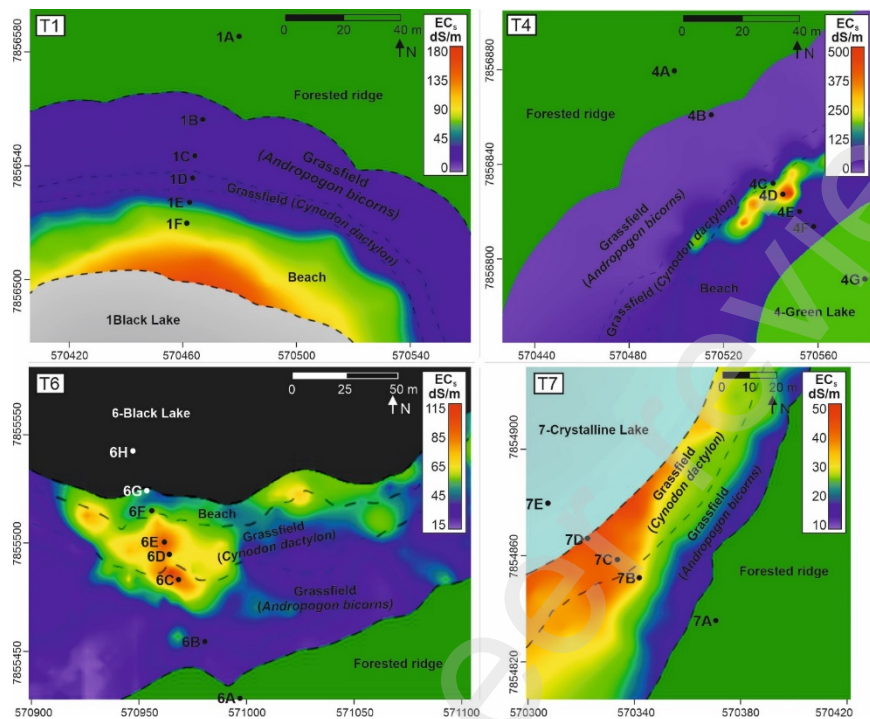
383

384 *Fig. 5. Topographic data - Altitude of ridges and lake levels measured on*  
 385 *the same day. Letters refer to points situated on the satellite view. (For*  
 386 *colour the reader is referred to the web version of this article).*

### 387 3.3. Toposequences

388 EC<sub>s</sub> mapping around toposequences and borehole  
 389 locations are given in Fig. 6. Several factors can result in  
 390 higher EC values, such as soil moisture, clay content, and  
 391 concentration of ionic species in the soil solution (Alves et  
 392 al., 2013). For better visualization, the EC<sub>s</sub> profiles along  
 393 each toposequence will be shown in toposequence figures  
 394 (red lines on Figs. 8 to 11).

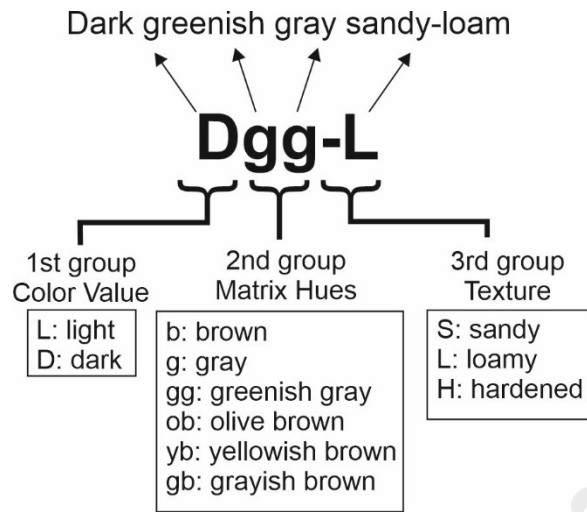




395

396 *Fig. 6. Apparent electrical conductivity mapping of soils – EC<sub>s</sub> values*  
 397 *around each saline-alkaline lake selected, with the delimitation of*  
 398 *different landscape unit areas and the positioning of all boreholes. (For*  
 399 *colour the reader is referred to the web version of this article).*

400 The nomenclature of the horizons is made according  
 401 to their dominant color and their texture, following the rules  
 402 presented in Fig. 7, with notes being taken about horizons  
 403 with heterogeneous colors, varied nodules, and spots  
 404 associated with organic matter. Details about borehole  
 405 positioning, depths, particle size distribution and pH in water  
 406 for all samples are available as supplementary material.

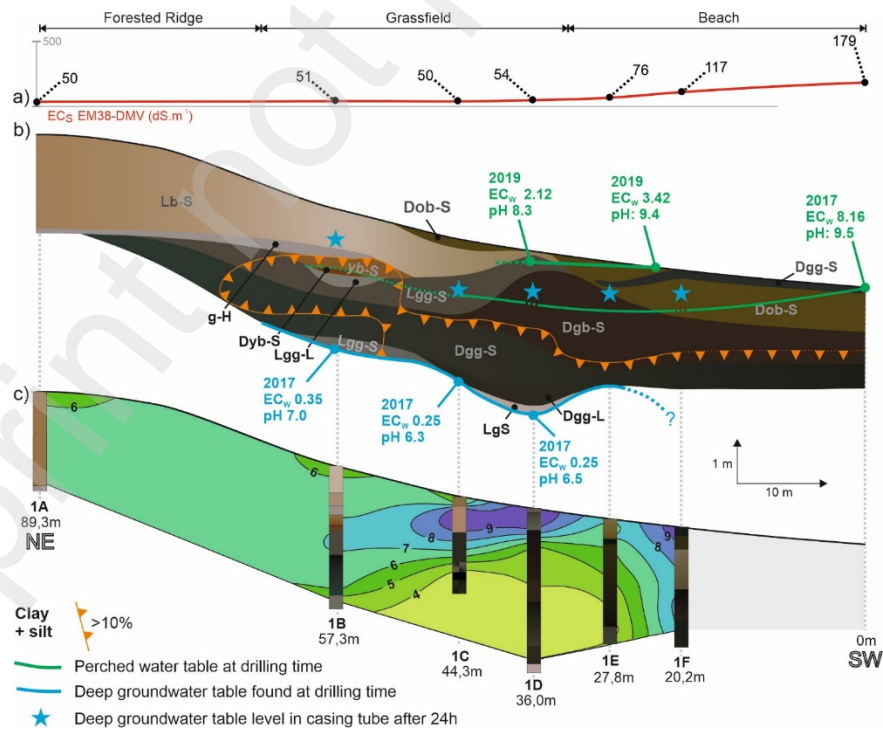


407

408 *Fig. 7. Nomenclature of the horizons – Scheme of the different color*  
 409 *values, matrix hues and textures found in the studied soils.*

410

**3.3.1. T1-Black lake toposequence (Fig. 8)**



411

412 *Fig. 8. T1 - Main characteristics of the 1-Black lake toposequence. (a)*  
413 *EC<sub>S</sub> profile; (b) soil horizons, water levels, fine fraction and EC<sub>W</sub> values;*  
414 *c) soil pH. (For colour the reader is referred to the web version of this*  
415 *article).*

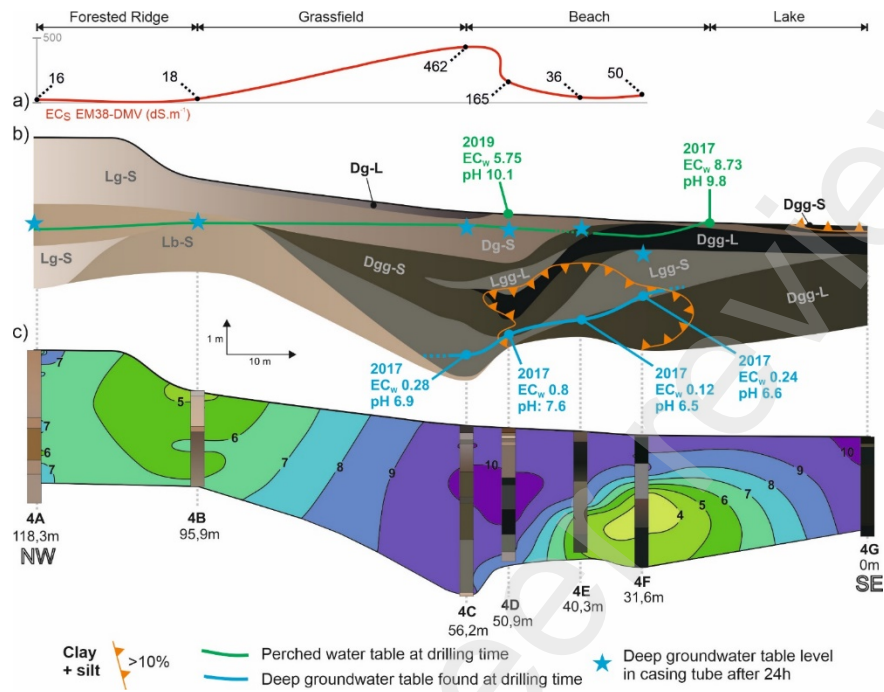
416           The ridge soil was a homogeneous, sandy, light  
417 brown profile more than 2 m deep overlying a g-H indurated  
418 silcrete horizon that prevented manual drilling. Such silcrete  
419 are known to form by Si liberation by silicate weathering,  
420 followed by its precipitation as secondary silica driven by  
421 supersaturation promoted by evaporation in the capillary  
422 fringe (Nash and Ulliyott, 2007). The geochemical feasibility  
423 of this process in the considered soil has been confirmed by  
424 modeling (Merdy et al., 2022). Downslope, this silcrete  
425 horizon progressively turned less indurated and  
426 disappeared, with the whole profile becoming darker and  
427 greener. The deep horizons, although remaining sandy,  
428 gradually became loamier, up to 17.6% of (clay + silt) at the  
429 base of the slope. These loamier horizons had low hydraulic  
430 conductivity, as evidenced by the two different water tables  
431 observed during the surveys: a perched water table with high  
432 EC<sub>W</sub> and pH (higher than 2.1 mS cm<sup>-1</sup> and 8.2, respectively),  
433 and a deep-water table with low EC<sub>W</sub> and pH (lower than 0.4

434 mS cm<sup>-1</sup> and 7.1, respectively). The deep-water table was  
435 under hydraulic load: water slowly raised in the casing tube  
436 after it was reached. The low-permeability green horizons  
437 formed a marked step on the slope, favoring the hydraulic  
438 discontinuity between the ridge and the soils of the lower  
439 slope.

440 Soil pH (Fig. 8c) ranged from 3 to 10 within the  
441 toposequence. Ridge soil was slightly acidic, around 6-7.  
442 Topsoil horizons gradually became more alkaline  
443 downstream, reaching values greater than 9 in the lower part  
444 of the slope, which was consistent with the gradual increase  
445 of EC<sub>s</sub>. Very acid horizons (hyperacidic horizons, pH < 4)  
446 were observed at depth in the lower third of the slope.

447 Horizon geometry and characteristics, including pH  
448 contrast, have already been observed in similar  
449 toposequences (Barbiero et al., 2008, 2016). Based on  
450 geochemical modeling, the pH contrast was attributed by  
451 Merdy et al. (2022) to the mixing of alkaline water from  
452 downslope surface horizons and deep acidic groundwater.

453 3.3.2. *T4-Green lake toposequence (Fig. 9)*



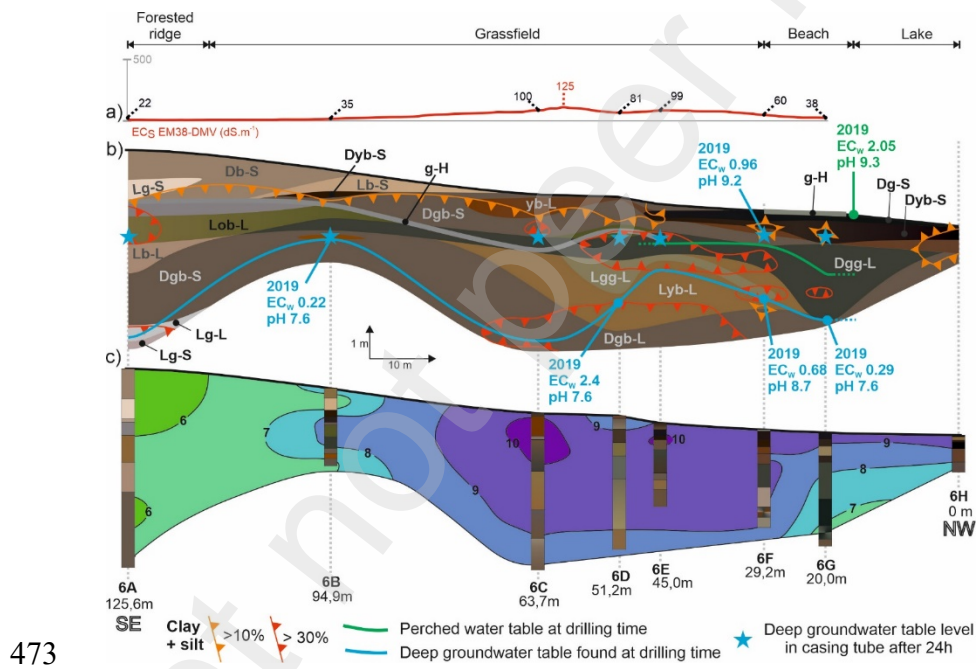
454

455 *Fig. 9. T4 - Main characteristics of the 4-Green lake toposequence. (a)*  
 456 *EC<sub>s</sub> profile; (b) soil horizons, water levels, fine fraction and EC<sub>w</sub> values;*  
 457 *(c) soil pH. (For colour the reader is referred to the web version of this*  
 458 *article).*

459 The T4 toposequence was very similar to the T1  
 460 toposequence: from the upper to the lower part of the slope,  
 461 the profile progressively darkens and turns greener; (clay +  
 462 silt) content increase in depth forming low hydraulic  
 463 conductivity horizons isolating an alkaline perched water  
 464 table from acidic deep groundwater; topsoil pH increases  
 465 gradually up to 10.5; and there are hyperacidic horizons at  
 466 depth in the lower third of the slope. There were, however,

467 some differences: no indurated silcrete was observed at  
 468 depth in the ridge soil; the  $EC_S$  profile showed high values  
 469 towards the middle of the slope, which could be due to a  
 470 local higher accumulation of salts in topsoil horizons by  
 471 capillary rise of the lake water.

472 **3.3.3. T6-Black lake toposequence (Fig. 10)**



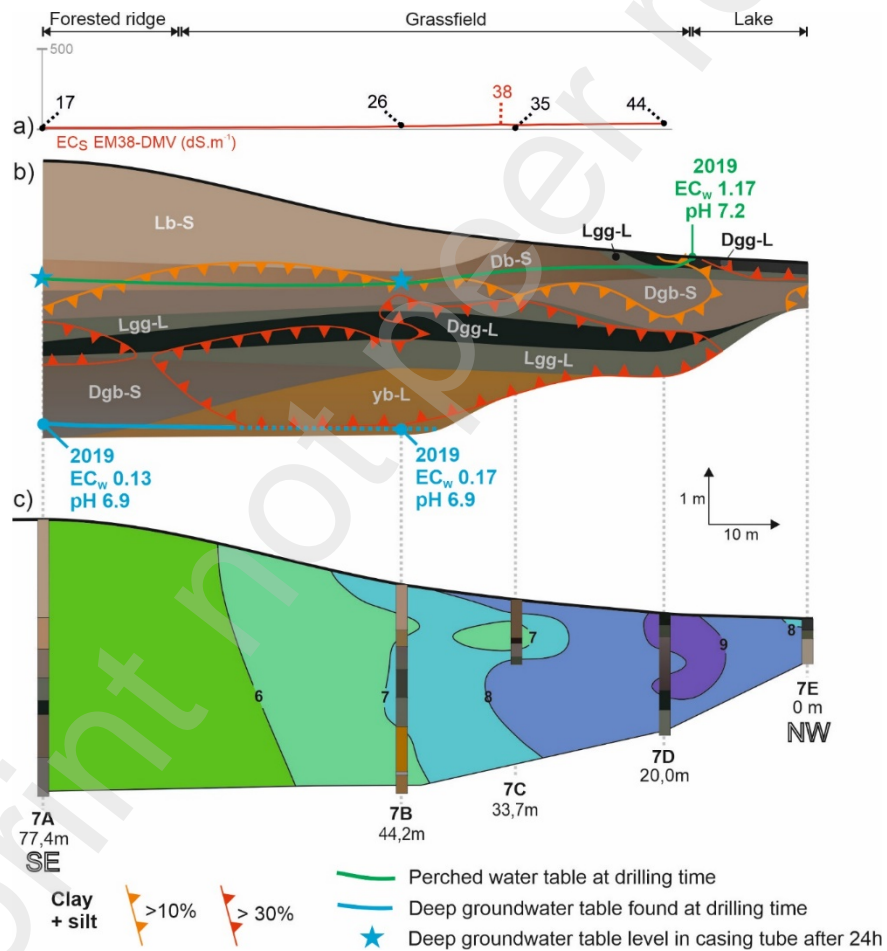
474 Fig. 10. T6 - Main characteristics of the 6-Black lake toposequence. (a)  
 475  $EC_S$  profile; (b) soil horizons, water levels, fine fraction and  $EC_W$  values;  
 476 (c) soil pH. (For colour the reader is referred to the web version of this  
 477 article).

478 Most of the similarities between T1 and T4  
 479 toposequences were observed in the T6 toposequence:

480 horizon color transitions, (clay + silt) content increase  
481 forming low hydraulic conductivity horizons that isolate  
482 different water tables and a gradual increase of the topsoil  
483 pH. However, some features differed. The deep groundwater  
484 was slightly less acidic (around 7.6), which could indicate  
485 less impermeable green horizons. The whole sequence had  
486 a higher (clay + silt) fraction content, which could be due to a  
487 higher fine fraction content of the parent material, as  
488 suggested by a (silt + clay) content higher than 30%, 550 cm  
489 deep, in the ridge soil. A well-developed hardened silcrete  
490 horizon was observed around 150 cm in depth from the ridge  
491 to the lower third of the slope and discontinuous topsoil  
492 silcrete horizons were also observed along the lower third of  
493 the slope. Better development of silcrete compared to the T1  
494 toposequence could be due to higher capillary rise due to  
495 the higher content of the fine fraction or, regarding the ridge  
496 silcrete, a flow-barrier effect due to textural layering (Li et al.,  
497 2014). The  $EC_s$  profile along the slope presented multiple  
498 peaks, which could be related to textural variations in the  
499 topsoil horizons. Acidic, not hyperacidic, horizons were  
500 observed at depth in the lower part of the toposequence,  
501 which can be due to less impermeable green horizons

502 allowing better mixing between alkaline and acid  
 503 groundwaters and better water turnover. It is also possible  
 504 that the observations were not deep enough to observe  
 505 hyperacidity.

506 3.3.4. T7-Crystalline toposequence (Fig. 11)



507  
 508 Fig. 11. T7 - Main characteristics of the 7-Crystalline lake toposequence.  
 509 (a)  $EC_s$  profile; (b) soil horizons, water levels, fine fraction and  $EC_w$



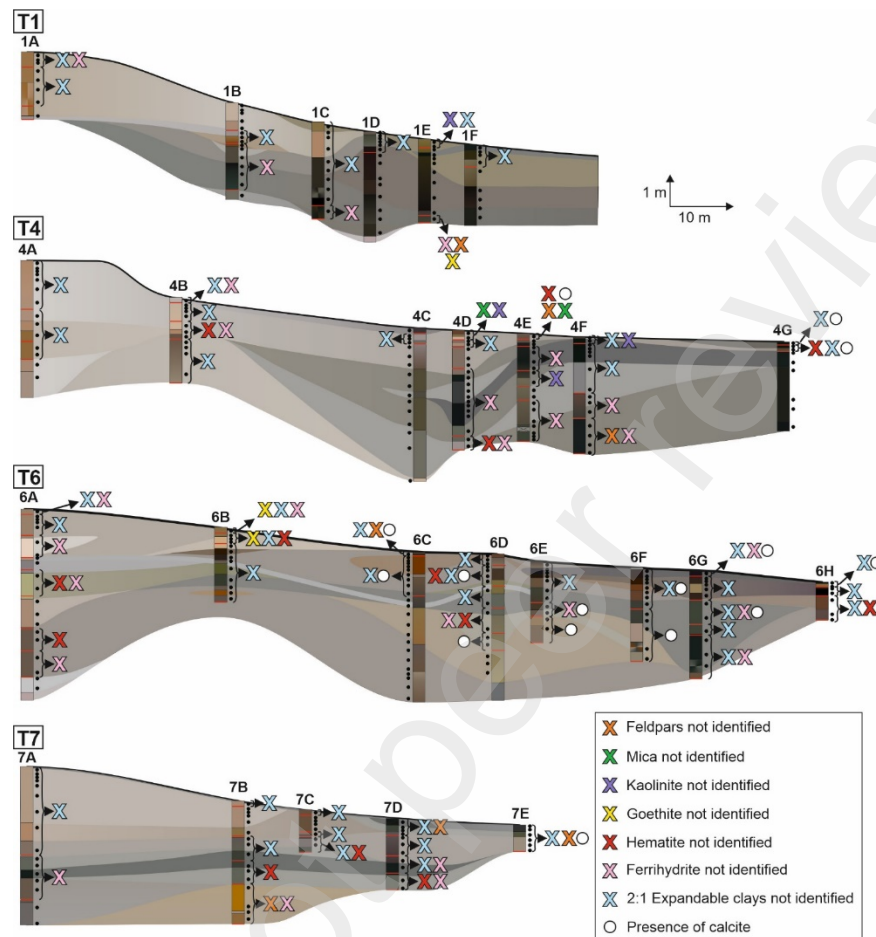
510 values; c) soil pH. (For colour the reader is referred to the web version of  
511 this article).

512           The T7 toposequence ends on a less alkaline lake  
513 than the others, with the presence of shells on the beach  
514 surface and subaerial vegetation inside the lake. Like the  
515 other three toposequences, this one had soils ranging from  
516 acidic to alkaline horizons from the ridge to the lake and two  
517 distinct water tables separated by greenish horizons. The  
518 poorly permeable green horizons, however, did not form a  
519 marked step on the slope. The hydraulic discontinuity  
520 between the ridge soils and the upper soil horizons at the  
521 lower part of the slope is therefore less marked than for the  
522 other sequences. The downslope soils were slightly less  
523 alkaline than in other toposequences, with the maximum  
524 measured pH being 9.2. Consistently, the pH of the perched  
525 water table measured in 2019 had a lower  $EC_w$  value (1.1  
526  $mS\ cm^{-1}$ ) than in other toposequences and was only slightly  
527 alkaline (7.2), with little difference with the deep groundwater  
528 (6.9). No hyperacidic horizons were observed at depth in the  
529 lower part of the toposequence. As for toposequence T7, the  
530 soils showed, on average, a higher fine fraction content than  
531 toposequence T1 and T4. As for the T7 toposequence, the

532 less intense peaks in the ECs profile along the slope could  
533 be related to horizons with less salt accumulation, in which  
534 less textural variations in the topsoil horizons causes less  
535 confinement.

#### 536 **3.4. Mineralogy results**

537 A summary of main minerals identified by XRD, FTIR  
538 and DRS is given in Fig. 12. The main minerals identified  
539 along the toposequences were quartz, feldspars (microcline  
540 and/or orthoclase), micas (muscovite and/or illite), kaolinite,  
541 2:1 expandable clay minerals (montmorillonite and/or  
542 vermiculite), calcite, goethite, hematite, ferrihydrite.



543

544 Fig. 12. Soil mineralogy - Main minerals along the sequences. Black  
 545 points indicate the analyzed samples. Unless otherwise stated, the  
 546 following minerals have been identified at each point: quartz, feldspars,  
 547 micas, kaolinite, 2:1 expandable clay minerals, goethite, hematite,  
 548 ferrihydrite. The figure therefore represents the absence of one or more  
 549 of these minerals or the presence of calcite. (For colour the reader is  
 550 referred to the web version of this article).

551

Quartz, feldspar and muscovite, part of illite and

552

kaolinite are inherited from the parent sediment. These

553 minerals were likely transported with little modification and  
554 remained restricted to the sand and silt fractions (Assine et  
555 al., 2015; Oliveira Júnior et al., 2020).

556           According to published studies on similar systems  
557 (Barbiero et al., 2008, 2016; Furquim et al., 2008, 2010a,  
558 2010b; Guerreiro et al., 2019; Andrade et al., 2020), the  
559 main expected secondary minerals are Fe-kaolinite, Fe-illite,  
560 Fe-beidellite-type smectite in upslope soils, stevensite-type  
561 smectite in downslope soils, with many types of mixed-  
562 layered types from these phyllosilicate species, amorphous  
563 silica which can form silcrete nodules or horizons, and  
564 calcite. In this study we did not differentiate illite from  
565 muscovite, or types of expandable 2:1 clays. We have  
566 however noticed that expandable clays were present  
567 everywhere, except in the sandiest horizons of the upper  
568 part of the profiles. On ridges, this was expected in the  
569 leached, acidic sandy horizons where there are no  
570 conditions for the neoformation of 2:1 secondary clay  
571 minerals. On slopes, where higher pH and local carbonate  
572 precipitations attest to more confined conditions, possibly  
573 precipitated 2:1 minerals may be leached at depth or  
574 downstream by perched groundwater circulation.

575            Calcite was observed in high pH downslope  
576 horizons, especially in the T6 toposequence, where HCl-  
577 effervescent nodules larger than 2 mm were observed.  
578 Calcite in the other green horizons could however have been  
579 ignored due to the method of separation of the clay fraction  
580 during which soluble minerals can be dissolved (§2.4).  
581 Calcite nodules support the hypothesis of concentration of  
582 solutes by dry season evaporation of groundwater  
583 presumably from the lake or from deeper horizons.

584            Amorphous silica was not identified by XRD, but its  
585 presence is most likely based on observations of hardened  
586 horizons (g-H) or non-HCl-effervescent nodules (horizons  
587 Dgg-L and Lgg-L).

588            These results are consistent with the results  
589 obtained by Merdy et al. (2022) using conceptual  
590 geochemical modeling on an idealized toposequence similar  
591 to those described here. While kaolinite precipitation is  
592 generally associated with wetter climates (Ishida et al.,  
593 2014), this remains possible here despite the strongly  
594 negative annual water balance. These authors, however  
595 predict, in the downslope surface horizons, that there is  
596 precipitation of evaporitic minerals (gaylussite, pirssonite,

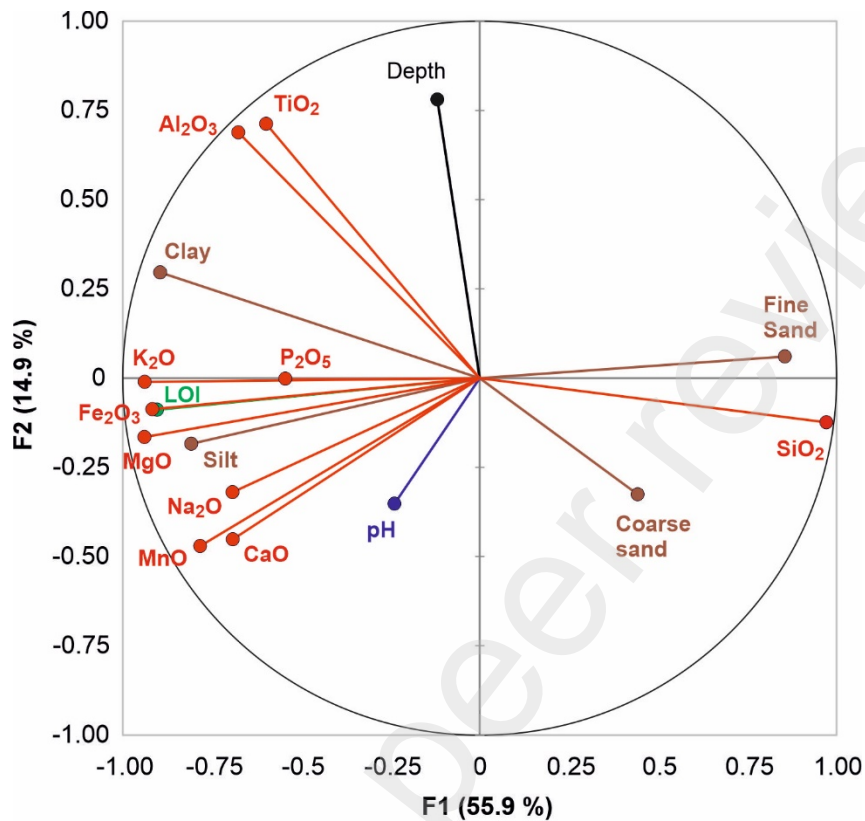
597 sylvite, nahcolite, halite, glaserite), none of which were  
598 observed in our study. Here too, the mode of preparation of  
599 the clay fraction is probably responsible for the non-  
600 observation of these very soluble minerals.

601           With regard to iron oxides and hydroxides, we did  
602 not observe in the results obtained here a correlation of their  
603 distribution with other characteristics nor a causality in this  
604 distribution. Goethite and hematite are common phases in  
605 soils, as a result of Fe-rich silicates weathering processes  
606 and may even act as a reliable proxy for local precipitation  
607 (Zhang et al., 2007). While hematite can be associated with  
608 hot and dry environments, goethite can be associated with  
609 cold and humid environments. Ferrihydrite ( $\text{Fe}^{3+}_2\text{O}_3 \cdot 0.5\text{H}_2\text{O}$ )  
610 is a metastable mineral that marks the first precipitation  
611 stage in iron oxidation during hydrolysis, which may  
612 transform via the hematite or goethite transformation  
613 pathways depending on pH and moisture. Such  
614 transformations occur simultaneously, either by the  
615 condensation of ions or crystal dissolution in acidic (pH 3 to  
616 4) and alkaline (pH > 8) conditions forming goethite, or by  
617 dehydration and internal atomic rearrangement of solid  
618 ferrihydrite in a neutral pH favoring hematite formation

619 (Schwertmann et al., 1999; Cudennec and Lecerf, 2006). In  
620 the studied toposequences, such dynamics were not  
621 detected between hyperacid (pH < 4) and alkaline zones.

### 622 **3.5. Chemical results**

623 The average of all samples demonstrates the  
624 following succession: silica ( $\text{SiO}_2 = 91.84\%$ ), aluminum  
625 ( $\text{Al}_2\text{O}_3 = 2.22\%$ ), iron ( $\text{Fe}_2\text{O}_3 = 1.75\%$ ), potassium ( $\text{K}_2\text{O} =$   
626  $0.75\%$ ), calcium ( $\text{CaO} = 0.30\%$ ), magnesium ( $\text{MgO} =$   
627  $0.21\%$ ), titanium ( $\text{TiO}_2 = 0.18\%$ ), sodium ( $\text{Na}_2\text{O} = 0.11\%$ ),  
628 manganese ( $\text{MnO} = 0.11\%$ ) and phosphorus ( $\text{P}_2\text{O}_5 =$   
629  $0.01\%$ ). The great dominance of  $\text{SiO}_2$  is due to the high  
630 content of quartz sand in all samples. Relationships between  
631 the elements and the soil material texture and pH can be  
632 discussed from the PCA results (Fig. 13).



633

634 *Fig. 13. Statistical data - PCA correlation circle between variables.*

635 Percentage on each factorial axis gives the explained variance. LOI: loss  
 636 on ignition.

637 The first factorial axis is mainly defined by SiO<sub>2</sub> and

638 sand on one side, and clay, silt and other elements on the

639 other side. This is consistent with the differentiation between

640 very sandy horizons and horizons with the presence of clay,

641 often associated with other minerals (calcite, iron oxides).

642 The second factorial axis is mainly defined by depth, Al<sub>2</sub>O<sub>3</sub>643 and TiO<sub>2</sub> on one side, opposed to pH, CaO, MnO and Na<sub>2</sub>O



644 on the other side. The negative correlation between pH and  
645 depth is driven by high pH surface horizons near the lake  
646 and hyperacidic horizons at depth in the T1 and T4  
647 sequences. The axis probably also differentiates acidic  
648 horizons richer in aluminous 1:1 clays (kaolinite) as indicated  
649 by the  $\text{Al}_2\text{O}_3$  point, alkaline horizons richer in less aluminous  
650 2:1 clays with K, Fe or Mg (Fe-illite, stevensite) as indicated  
651 by the  $\text{K}_2\text{O}$ ,  $\text{Fe}_2\text{O}_3$  and  $\text{MgO}$  points and evaporitic horizons  
652 as indicated by the  $\text{Na}_2\text{O}$  and the  $\text{CaO}$  points.

### 653 **3.6. Possible active processes**

654 The granulometric, mineralogical and chemical  
655 differences in the soils observed along each toposequence  
656 are the result of neoformation, precipitation, dissolution,  
657 transformation, dehydration and mineral heritage acting on  
658 the site (Macias and Camps, 2020; Vidoca, 2020), all  
659 dependent on physicochemical properties of the soil  
660 solutions.

#### 661 *3.6.1. Pedogenesis, hydrodynamics and lake type*

662 The observed mineralogy reflects particularities of  
663 the Nhecolândia environment. Firstly, that there is a  
664 predominance of sandy materials, therefore very siliceous,

665 with low levels of aluminum and good permeability.  
666 Secondly, the contrasting climate allows both a leaching  
667 environment during the rainy season with solute supply in  
668 lakes, and a confined environment during the dry season  
669 with solute accumulation in lakes and downslope soils.  
670 Annual precipitation and potential evapotranspiration in the  
671 region (averages of 1100 and 1400 mm, respectively) result  
672 in a negative water balance (Alho, 2008). However, during  
673 rainy seasons, precipitation exceeds potential  
674 evapotranspiration by about 200 mm and, consequently, a  
675 water deficit of about 500 mm is maintained during the dry  
676 season (Hamilton et al., 1998). Thirdly, the fluctuations in  
677 water levels throughout the climate cycle are decisive. For  
678 freshwater lakes (*baías*), high water levels during the rainy  
679 season allows flushing towards main watercourses, of the  
680 solutes accumulated during the rainy season. Two non-  
681 exclusive processes can lead to flushing: lake overflow or  
682 deep leaching through groundwater (Sakamoto et al., 2004).  
683 Saline-alkaline lakes can form when low-permeability  
684 horizons allow hydraulic disconnection between deep  
685 groundwater on one hand, and lakes and downslope  
686 perched water-tables on the other. Here we confirmed the

687 presence of such horizons in each of the studied  
688 toposequences. We observed consistency between (1) the  
689 distribution of greenish, more clayey horizons and (2) the  
690 disconnection between an alkaline, perched groundwater  
691 and an acidic, deep groundwater. An overflow of non-  
692 alkaline groundwater continuing to feed the saline-alkaline  
693 lake during the dry season, as hypothesized by Costa et al.  
694 (2015), was not observed. On slopes, the greenish horizons  
695 formed a step favoring endorheism in T1, T4 and T6. A step  
696 was less visible in T7. It is therefore possible that the  
697 hydraulic isolation of the T7 crystalline lake has been less  
698 effective than for the other lakes, which could explain a lower  
699 confinement resulting in a lower alkalinity, attested by a  
700 lower EC<sub>w</sub> and pH of the lake waters. These would neither  
701 reach the threshold for triggering an algal bloom as in the  
702 green lakes, nor the threshold for massive solubilization of  
703 organic matter as in the black lakes.

#### 704 3.6.2. *Hydrodynamics and mineral genesis*

705 The type of minerals observed at the sequence  
706 scale was closely related to hydrodynamics that impacts the  
707 chemistry of the groundwater. The minerals observed here

708 where feldspar, 1:1 clays, non-expandable 2:1 phyllosilicate,  
709 expandable 2:1 clays, secondary silica, iron oxides and  
710 calcite. The mineral distribution observed at the  
711 toposequence scale is consistent with studies conducted in  
712 similar systems (Barbiero et al., 2008, 2016; Furquim et al.,  
713 2008, 2010a, 2010b). On the ridges, leached sandy horizons  
714 overlie horizons in which there is dissolution of primary  
715 minerals and neof ormation of minerals 1:1 (Fe-kaolinite) and  
716 2:1 (Fe-illite, Fe-beidellite). The greenish horizons on  
717 downslopes were formed by neoformations characteristic of  
718 confined environments (stevensite like clays, calcite). Our  
719 data provide new insights into the precipitation conditions of  
720 secondary silica. Secondary silica forming silcrete materials  
721 can form when there is not enough Al with regard to Si to  
722 allow phyllosilicate precipitation (Taylor and Eggleton, 2017).  
723 Here silcrete were observed (1) below the leached sandy  
724 horizons, on the ridge and in the upper part of the slope, or  
725 (2) on the topsoil, downslope. The first type of silcrete was  
726 formed in acidic ( $\text{pH} < 7$ ), sandy material. Silica precipitated  
727 from a soil water concentrated by evaporation in the capillary  
728 fringe, the low Si/Al ratio being likely since the percolating  
729 rainwater only encountered very sandy materials. The

730 second type of silcrete was formed in alkaline (pH > 9)  
731 material. Silica was precipitated from lake water transferred  
732 by capillarity and concentrated by evaporation. In this  
733 environment, the high Si/Al ratio is also favored by the high  
734 pH of the lake water that increases the quartz solubility and  
735 the quartz dissolution rate. The quartz dissolution rate is  
736 increased by 10 times at pH 9.5 compared to pH 7 (House  
737 and Orr, 1992) and by more than 20 times at the ionic  
738 strength of lake water compared to rainwater (Icenhower and  
739 Dove, 2000). As a result, the black lake water concentrations  
740 of dissolved Si and Al average about  $1.1 \cdot 10^{-1}$  and  $1.5 \cdot 10^{-4}$  ml  
741 L<sup>-1</sup>, respectively (Merdy et al., 2022). There are therefore two  
742 types of silcrete in such systems, one formed under  
743 neutral/acidic conditions, the other under alkaline conditions,  
744 both formed in an evaporating capillary fringe.

#### 745 **4. CONCLUSIONS**

746 This research marks the initial stage of the studies of  
747 factors that determine the dynamics between different types  
748 of saline-alkaline lakes and nearby surrounding soils. The  
749 objective of verifying, on a single site, a set of results  
750 previously acquired by independent studies on many distinct

751 Nhecolândia sites has been partially achieved. Our results  
752 confirmed the general organization of the soil cover around  
753 saline-alkaline lakes. The very sandy light brown soils of the  
754 ridges, which eventually present a silcrete type horizon at  
755 depth, give way down the slopes to greenish soils with, at  
756 depth, more clayey horizons with low permeability. These  
757 establish a hydraulic discontinuity between the slightly acidic  
758 groundwater of the general, deep groundwater and the very  
759 alkaline perched groundwater. Our 45-month time sequence  
760 of satellite data confirmed that the studied saline-alkaline  
761 lakes remained isolated from the ephemeral superficial flood  
762 channels. Some freshwater lakes, however, also remained  
763 isolated, which shows that the leaching of labile elements  
764 out of the lake catchment can occur via other processes than  
765 surface flushing, such as deep drainage or groundwater  
766 flushing. This shows that hydraulic discontinuity between  
767 surface groundwater on lake slopes and deep groundwater  
768 is a necessary condition for the acquisition of the saline-  
769 alkaline character of the lakes. Our results also suggested  
770 that some saline-alkaline lakes may remain crystalline due to  
771 slightly lower alkalinity as a result of less efficient hydraulic  
772 discontinuity between deep groundwater and alkaline lake

773 and soil water. The alkalinity of crystalline lakes would  
774 remain too low to allow a cyanobacteria bloom or the  
775 maintenance of organic matter in solution.

776 The present study confirmed the presence and  
777 location on the slopes of hyperacidic horizons, located  
778 downslope beneath the more alkaline horizons. Modeling by  
779 Merdy et al. (2022) showed that a pH between 3.2 and 3.5  
780 can be achieved by mixing water from alkaline horizons or  
781 lakes and deep groundwater, with the reduction in pH  
782 attributed to ferrollysis. The validation of such a mechanism  
783 will however require more detailed mineralogical  
784 investigations. It also remains to verify the mineralogy of 2:1  
785 minerals associated with deep ridge soil horizons and slope  
786 alkaline horizons.

#### 787 **DECLARATION OF INTERESTS**

788 The authors declare that they have no known  
789 competing financial interests or personal relationships that  
790 could have appeared to influence the work reported in this  
791 paper.

#### 792 **DATA AVAILABILITY**

793 Raw data is given as supplementary material.

794 **ACKNOWLEDGEMENTS**

795 This work was supported by the São Paulo  
796 Research Foundation (FAPESP) [grant numbers  
797 #2016/14227-5 and #2019/21157-1] and the Brazilian  
798 National Council for Scientific and Technological  
799 Development (CNPq) [grant number CRM #307024/2018-0].

800 **REFERENCES**

- 801 Acevedo, N.I.A., Rocha, M.C.G., Bertolino, L.C. 2017.  
802 Mineralogical characterization of natural clays from  
803 Brazilian Southeast region for industrial applications.  
804 Cerâmica, 63, 253-262. [http://dx.doi.org/10.1590/0366-](http://dx.doi.org/10.1590/0366-69132017633662045)  
805 [69132017633662045](http://dx.doi.org/10.1590/0366-69132017633662045)
- 806 Alho, C. J. R., 2008. Biodiversity of the Pantanal: response  
807 to seasonal flooding regime and to environmental  
808 degradation. Braz. J. Biol. 68 (4 suppl), 957–966.  
809 <https://doi.org/10.1590/S1519-69842008000500005>
- 810 Almeida, T. I. R. A., Fernandes, E., Mendes, D., Branco,  
811 F.C., Sígolo, J.B., 2007. Distribuição espacial de  
812 diferentes classes de Lagoas no Pantanal da  
813 Nhecolândia, MS, a partir de dados vetoriais e SRTM:



814 uma contribuição ao estudo de sua compartimentação e  
815 gênese. Geologia USP. v 7, n 2.

816 <https://doi.org/10.5327/Z1519-874x2007000200007>

817 Alves, S.M.F., Alcântara, G.R., Reis, E.F., Queiroz, D.M.,  
818 Valente, D.S.M., 2013. Definição de zonas de manejo a  
819 partir de mapas de condutividade elétrica e matéria  
820 orgânica. Biosciencia Journal, Uberlândia, v. 29, p. 104-  
821 114. Available from:

822 [https://seer.ufu.br/index.php/biosciencejournal/article/view](https://seer.ufu.br/index.php/biosciencejournal/article/view/13687)  
823 [/13687](https://seer.ufu.br/index.php/biosciencejournal/article/view/13687).

824 Anderson, J.U., 1963. An improved pretreatment for  
825 mineralogical analysis of samples containing organic  
826 matter. Clays Clay Miner. 10, 380–388.

827 <https://doi.org/10.1346/CCMN.1961.0100134>

828 Andrade, G.R.P., Furquim, S.A.C., Nascimento, T.T.V.,  
829 Brito, A.C., Camargo, G.R., Souza, G.C., 2020.

830 Transformation of clay minerals in salt-affected soils,  
831 Pantanal wetland, Brazil. Geoderma. 371, 114380.

832 <https://doi.org/10.1016/j.geoderma.2020.114380>

- 833 Assine, M.L., Merino, E.R., Pupim, F.N., Warren, L.V.,  
834 Guerreiro, R.L., McGlue, M.M., 2015. Geology and  
835 Geomorphology of the Pantanal Basin. In: Bergier, I. and  
836 Assine, M. L. (Eds.) Dynamics of the Pantanal Wetland in  
837 South America, pp. 23-50.  
838 [https://doi.org/10.1007/698\\_2015\\_349](https://doi.org/10.1007/698_2015_349)
- 839 Barbiero, L., Queiroz-Neto, J.P., Ciornei, G., Sakamoto,  
840 A.Y., Capellari, B., Fernandes, E., Vallès, V., 2002.  
841 Geochemistry of water and ground water in the  
842 Nhecolândia, Pantanal of Mato Grosso, Brazil: variability  
843 and associated processes. *Wetlands* 22 (3), 528–540.  
844 [https://doi.org/10.1672/0277-](https://doi.org/10.1672/0277-5212(2002)022[0528:GOWAGW]2.0.CO;2)  
845 [5212\(2002\)022\[0528:GOWAGW\]2.0.CO;2.](https://doi.org/10.1672/0277-5212(2002)022[0528:GOWAGW]2.0.CO;2)
- 846 Barbiero, L., Rezende-Filho, A.T., Furquim, S.A.C., Furian,  
847 S., Sakamoto, A.Y., Vallès, V., Graham, R.C., Fort, M.,  
848 Ferreira, R.P.D., Queiroz-Neto, J.P., 2008. Soil  
849 morphological control of hydrogeochemistry in a saline  
850 and freshwater lake landscape in the Pantanal of  
851 Nhecolândia, Brazil. *Geoderma*, 148, 91-106.  
852 <https://doi.org/10.1016/j.geoderma.2008.09.010>

853 Barbiero, L., Berger, G., Rezende Filho, A.T. Meunier, J-F.,  
854 Martins-Silva, E.R., Furian, S. 2016. Organic Control of  
855 Dioctahedral and Trioctahedral Clay Formation in an  
856 Alkaline Soil System in the Pantanal Wetland of  
857 Nhecolândia, Brazil. PLoS One, Jul 27, 11(7):e0159972.  
858 <https://doi.org/10.1371/journal.pone.0159972>

859 Boulet, R., Humbel, F.-X., Lucas, Y., 1982. Analyse  
860 structurale et cartographie en pédologie. I- Prise en  
861 compte de l'organisation bidimensionnelle de la  
862 couverture pédologique : les études de toposéquences et  
863 leurs principaux apports à la connaissance des sols. Cah.  
864 ORSTOM, sér. Pédol. XIX, 309-321. Available from:  
865 <https://www.documentation.ird.fr/hor/fdi:03252>

866 Cornell, R. M., Schwertmann, U. 2000. Iron Oxides in the  
867 Laboratory: Preparation and Characterization. 2ed Ext.  
868 WILEY-VCH. Weinheim.

869 Costa, M.P.F., Telmer, K.H., Evans, T.L., Almeida, T.I.R.,  
870 Diakun, M.T., 2015. The lakes of the Pantanal: inventory,  
871 distribution, geochemistry, and surrounding landscape.

- 872 Wetlands Ecology and Management, 23: 19-39.  
873 <https://doi.org/10.1007/s11273-014-9401-3>
- 874 Cotta, S.R., Pellegrinetti, T.A., Andreote, A.P.D., Costa, J.S.,  
875 Sarmiento, H., Fiore, M.F., 2022. Disentangling the  
876 lifestyle of bacterial communities in tropical soda lakes.  
877 Scientific Reports, v. 12, art. 7939.  
878 <https://doi.org/10.1038/s41598-022-12046-2>
- 879 Cudennec, Y. C., Lecerf, A. 2006. The transformation of  
880 ferrihydrite into goethite or hematite, revisited. Journal of  
881 Solid State Chemistry 179 (2006) 716–722.  
882 <https://doi.org/10.1016/j.jssc.2005.11.030>
- 883 Cunha, N.G. 1980. Considerações sobre os solos da sub-  
884 região da Nhecolândia, Pantanal Mato-Grossense.  
885 Corumbá, EMBRAPA-EUPAE de Corumbá, Circular  
886 técnico, 1. Available from:  
887 <https://www.infoteca.cnptia.embrapa.br/handle/doc/78769>  
888 [7](#)
- 889 Curti-Martins, E.R.. 2012. Tipologia de Lagoas Salinas no  
890 Pantanal da Nhecolândia (MS). Thesis. Universidade de  
891 São Paulo, São Paulo. Available from:

- 892 <https://www.teses.usp.br/teses/disponiveis/8/8135/tde->  
893 [14012013-172446/pt-br.php](https://www.teses.usp.br/teses/disponiveis/8/8135/tde-14012013-172446/pt-br.php)
- 894 Ekosse, G.I.E. 2005. Fourier Transform Infrared  
895 Spectrophotometry and X-ray powder Diffractometry as  
896 Complementary Techniques in characterizing Clay size  
897 fraction of Kaolin. J. Appl. Sci. Environ. Mgt. Vol. 9 (2) 43-  
898 48. <https://doi.org/10.4314/jasem.v9i2.17289>
- 899 EMBRAPA, 2017. Manual de Métodos de Análise de Solo.  
900 (3ed ampl). Brasília. Available from:  
901 [https://www.embrapa.br/busca-de-publicacoes/-](https://www.embrapa.br/busca-de-publicacoes/-/publicacao/1085209/manual-de-metodos-de-analise-de-solo)  
902 [/publicacao/1085209/manual-de-metodos-de-analise-de-](https://www.embrapa.br/busca-de-publicacoes/-/publicacao/1085209/manual-de-metodos-de-analise-de-solo)  
903 [solo](https://www.embrapa.br/busca-de-publicacoes/-/publicacao/1085209/manual-de-metodos-de-analise-de-solo)
- 904 Freitas, J.G., Furquim, S.A.C., Aravena, R., Cardoso, E.L.,  
905 2019. Interaction between lakes' surface water and  
906 groundwater in the Pantanal wetland, Brazil. Env. Earth  
907 Sci. 78, 139. <https://doi.org/10.1007/s12665-019-8140-4>
- 908 Furian, S., Curti-Martins, E.R., Parizotto, T.M., Rezende-  
909 Filho A.T., Victoria, R.L., Barbiero, L., 2013. Chemical  
910 diversity and spatial variability in myriad lakes in  
911 Nhecolândia in the Pantanal wetlands of Brazil. Limnology

- 912 and Oceanography, 58: 2249-2261. Available from:  
913 <https://hal.archives-ouvertes.fr/hal-02043233>
- 914 Furquim, S.A.C., Graham, R.C., Barbiero, L., Queiroz-Neto,  
915 J.P., Vallès, V., 2008. Mineralogy and genesis of  
916 smectites in an alkaline-saline environment of Pantanal  
917 wetland, Brazil. Clays and Clay Minerals 56, 579- 595.  
918 <https://doi.org/10.1346/CCMN.2008.0560511>
- 919 Furquim, S.A.C., Graham, R.C., Barbiero, L., Queiroz-Neto,  
920 J.P., Vidal-Torrado, P., 2010a. Soil mineral genesis and  
921 distribution in a saline lake landscape of the Pantanal  
922 wetland, Brazil. Geoderma, 154, 518-528.  
923 <https://doi.org/10.1016/j.geoderma.2009.03.014>
- 924 Furquim, S.A.C., Barbiero, L., Graham, R.C., Queiroz-Neto,  
925 J.P., Ferreira, R.P.D., Furian, S., 2010b. Neoformation of  
926 micas in soils surrounding an alkaline-saline lake of  
927 Pantanal wetland, Brazil. Geoderma, 158, 331-342.  
928 <https://doi.org/10.1016/j.geoderma.2010.05.015>
- 929 Guerreiro, R. L. 2016. Mudanças paleoambientais no  
930 holoceno em lagoas salinas do Pantanal da Nhecolândia.  
931 Thesis. Universidade Estadual Paulista, Rio Claro.

- 932 Available from:  
933 <https://repositorio.unesp.br/handle/11449/147123>
- 934 Guerreiro, R.L., Bergier, I., McGlue, M.M., Warren, L.V.,  
935 Abreu, U.G.P., Abrahão, J., Assine, M.L., 2019. The soda  
936 lakes of Nhecolandia: a conservation opportunity for the  
937 Pantanal wetlands. *Perspect. Ecol. Conserv.* 17 (1), 9–18.  
938 <https://doi.org/10.1016/j.pecon.2018.11.002>.
- 939 GOOGLE. 2020. Google Earth Engine API. Available from  
940 <https://developers.google.com/earth-engine>. Accessed at  
941 June 2<sup>nd</sup>, 2020.
- 942 Hamilton, S.K., Souza, O.C., Coutinho, M.E., 1998.  
943 Dynamics of floodplain inundation in the alluvial fan of the  
944 Taquari River (Pantanal, Brazil). *SIL Proc.* 1922–2010  
945 (26), 916–922.  
946 <https://doi.org/10.1080/03680770.1995.11900852>
- 947 House, W. A., Orr, D.R., 1992. Investigation of the pH  
948 dependence of the kinetics of quartz dissolution at 25 C.  
949 *Journal of the Chemical Society, Faraday Transactions*,  
950 vol. 88, no 2, p. 233-241.  
951 <https://doi.org/10.1039/FT9928800233>

- 952 Icenhower, J. P., Dove, P. M., 2000. The dissolution kinetics  
953 of amorphous silica into sodium chloride solutions: effects  
954 of temperature and ionic strength. *Geochimica et*  
955 *Cosmochimica Acta*, 64(24), 4193-4203.  
956 [https://doi.org/10.1016/S0016-7037\(00\)00487-7](https://doi.org/10.1016/S0016-7037(00)00487-7)
- 957 INSTITUTO NACIONAL DE METEOROLOGIA - INMET.  
958 Banco de Dados Meteorológicos para Ensino e Pesquisa  
959 - BDMEP. Brasília, DF, Brasil, c2020. Disponível em:  
960 <http://www.inmet.gov.br/portal/index.php?r=bdmep/bdmep>  
961 . (accessed at 9 march 2020).
- 962 Ishida, D.A., Montes, C.R., Lucas, Y., Pereira, O.J.R.,  
963 Merdy, P., Melfi, A.J. 2014. Genetic relationships between  
964 ferralsols, podzols and white kaolin in Amazonia. *Eur. J.*  
965 *of Soil Sci*, 65, 706–717.  
966 <https://doi.org/10.1111/ejss.12167>
- 967 Jackson, M.L. 1985. Soil chemical analysis advanced  
968 course, 5<sup>th</sup> print. Department of Soil Science University,  
969 Wisconsin, Madison WI, 894p
- 970 Ji, J., Ge, Y., Balsam, W., Damuth, J.E., Chen, J., 2009.  
971 Rapid identification of dolomite using a Fourier Transform



- 972 Infrared Spectrophotometer (FTIR): A fast method for  
973 identifying Heinrich events in IODP Site U1308. Marien  
974 Geology. 258, 60-68.  
975 <https://doi.org/10.1016/j.margeo.2008.11.007>
- 976 Jolliffe, I.T. 2002 Principal component analysis. 2nd ed,  
977 Springer-Verlag, New York
- 978 Kosmas, C. S, Curi, N., Bryant, R.B., Franzmeier, D.P.,  
979 1984. Characterization of iron oxide minerals by second  
980 derivative visible spectroscopy. Soil Science Society of  
981 America Journal, v. 48, n. 2, p. 401-405.  
982 <https://doi.org/10.2136/sssaj1984.0361599500480002003>  
983 [6x](#)
- 984 Lainé, M., Balan, E., Allard, T., Paineau, E., Jeunesse, P.,  
985 Mostafavi, M., Robert, J.-L, Le Caër, S., 2017. Reaction  
986 mechanisms in swelling clays under ionizing radiation:  
987 influence of the water amount and of the nature of the clay  
988 mineral. RSC Advances, 7 (256), 526-534.  
989 <https://doi.org/10.1039/C6RA24861F>
- 990 Li, X., Chang, S. X., Salifu, K. F. 2014. Soil texture and  
991 layering effects on water and salt dynamics in the

- 992 presence of a water table: a review. Environmental  
993 reviews, 22(1), 41-50. [https://doi.org/10.1139/er-2013-](https://doi.org/10.1139/er-2013-0035)  
994 [0035](https://doi.org/10.1139/er-2013-0035)
- 995 Macías, F., Camps-Arbestain, M. 2020. A biogeochemical  
996 view of the world reference base soil classification  
997 system: Homage to Ward Chesworth. Advances in  
998 Agronomy, Volume 160.  
999 <https://doi.org/10.1016/bs.agron.2019.11.002>
- 1000 Mariot, M., Dudak, Y., Furian, S., Sakamoto, A., Vallès, V.,  
1001 Fort, M., Barbiero, L., 2007. Dissolved organic matter  
1002 fluorescence as a water flow tracer in the tropical wetland  
1003 of Pantanal of Nhecolândia, Brazil. Science of the Total  
1004 Environment. 388, 183–196.  
1005 <https://doi.org/10.1016/j.scitotenv.2007.08.003>
- 1006 Malengrau, N., Bedidi, A., Muller, J.-P., Herbillon, A.J., 1996.  
1007 Spectroscopic control of iron oxide dissolution in two  
1008 ferralitic soils. European Journal of Soil Science, v. 47,  
1009 p.13-20. [https://doi.org/10.1111/j.1365-](https://doi.org/10.1111/j.1365-2389.1996.tb01367.x)  
1010 [2389.1996.tb01367.x](https://doi.org/10.1111/j.1365-2389.1996.tb01367.x)

- 1011 Merdy, P., Gamrani, M., Montes, C.R., Rezende-Filho, A.T.,  
1012 Barbiero, L., Ishida, D.A., Silva, A.R.C., Melfi, A.J., Lucas,  
1013 Y., 2022. Processes and rates of formation defined by  
1014 modelling in alkaline to acidic soil systems in Brazilian  
1015 Pantanal wetland. *Catena*, 210, 105876.  
1016 <https://doi.org/10.1016/j.catena.2021.105876>
- 1017 Munsell Color (Firm). 1954. Munsell soil color charts.  
1018 Baltimore.
- 1019 Nash, D.J., Ulliyott, J.S., 2007. Silcrete. In: *Geochemical*  
1020 *Sediments and Landscapes*, Nash, D.J., McLaren, S.J.  
1021 (eds.). Oxford, UK, Blackwell Publishing, p. 95–148.  
1022 <https://doi.org/10.1002/9780470712917>
- 1023 Oliveira Júnior, J.C., Andrade, G.R.P., Barbiero, L., Furquim,  
1024 S.A.C., Vidal-Torrado, P., 2020. Flooding effect on  
1025 mineralogical and geochemical changes in alkaline-sodic  
1026 soil system of northern Pantanal wetlands. Brazil. *Eur. J.*  
1027 *Soil Sci.* 71 (3), 433–447.  
1028 <https://doi.org/10.1111/ejss.12871>

- 1029 Pansu, M., Gautheyrou, J., 2006. Particle size analysis. In:  
1030 Handbook of Soil Analysis. Springer, Berlin, Heidelberg,  
1031 pp. 15–63. [https://doi.org/10.1007/978-3-540-31211-6\\_2](https://doi.org/10.1007/978-3-540-31211-6_2)
- 1032 Pellegrinetti, T.A., Cotta, S.R., Sarmiento, H., Costa, J.S.,  
1033 Delbaje, E., Montes, C.R., Camargo, P.B., Barbiero, L.,  
1034 Rezende-Filho, A.T., Fiore, M.F., 2022. Bacterial  
1035 Communities Along Environmental Gradients in Tropical  
1036 Soda Lakes. Microbial Ecology.  
1037 <https://doi.org/10.1007/s00248-022-02086-6>.
- 1038 Pereira, O.J.R., Merino, E.R., Montes, C.R., Barbiero, L.,  
1039 Rezende-Filho, A.T., Lucas, Y., Melfi, A.J., 2020.  
1040 Estimating water pH using cloud-based landsat images for  
1041 a new classification of the Nhecolândia Lakes (Brazilian  
1042 Pantanal). Remote Sens. 12, 1090.  
1043 <https://doi.org/10.3390/rs12071090>
- 1044 PLANET LABS. 2016. Planet Imagery Product Specification.  
1045 São Francisco: Planet Labs, v. 56.
- 1046 Russell, J.D. and Fraser, A.R., 1994. Infrared Methods. In:  
1047 Wilson, M.J., Ed., Clay Mineralogy: Spectroscopic and  
1048 Chemical Determinative Methods, Chapman and Hall,

- 1049 London, 11-67. <http://dx.doi.org/10.1007/978-94-011->  
1050 [0727-3\\_2](http://dx.doi.org/10.1007/978-94-011-0727-3_2).
- 1051 Saikia, B.J., Parthasarathy, G., Sarmah, N.C., 2008. Fourier  
1052 transform infrared spectroscopic estimation of crystallinity  
1053 in SiO<sub>2</sub> based rocks. Bull. Mater. Sci., Vol. 31, No. 5,  
1054 775–779. <https://doi.org/10.1007/s12034-008-0123-0>
- 1055 Sakamoto, A.Y., Sakamoto, L.L.S., Neto, J.P.Q., Barbiero,  
1056 L., 2004. Abordagem metodológica para o estudo de  
1057 lagoas e Salinas do Pantanal da Nhecolândia, MS:  
1058 fazenda São Miguel do Firme. IV Simp. Sobre Rec. Nat. e  
1059 sócio-econômicos do Pantanal. Corumbá. Available from:  
1060 <https://docplayer.com.br/87510495-Abordagem->  
1061 [metodologica-para-o-estudo-de-lagoas-e-salinas-do-](https://docplayer.com.br/87510495-Abordagem-)  
1062 [pantanal-da-nhecolandia-ms-fazenda-sao-miguel-do-](https://docplayer.com.br/87510495-Abordagem-)  
1063 [firme.html](https://docplayer.com.br/87510495-Abordagem-)
- 1064 Salis, S.M., Lehn, C.R., Mattos, P.P., Bergier, I., Crispim,  
1065 S.M.A., 2014. Root behavior of savanna species in  
1066 Brazil's Pantanal wetland. Glob. Ecol. Conserv. 2, 378–  
1067 384. <https://doi.org/10.1016/j.gecco.2014.10.009>.

- 1068 Scheinost, A.C., Chavernas, A., Barrón, V., Torrent, T.,  
1069 1998. Use and limitations of second-derivative diffuse  
1070 reflectance spectroscopy in the visible to near-infrared  
1071 range to identify and quantify Fe oxide minerals in soils.  
1072 Clays and Clay Minerals, v. 46, n. 5, p. 528-536.  
1073 <https://doi.org/10.1346/CCMN.1998.0460506>
- 1074 Schwertmann, U., Friedl, J., Stanjek, H., 1999. From Fe(III)  
1075 ions to Ferrihydrite and then to Hematite. Colloid Interface  
1076 Sci. 209, 215. <https://doi.org/10.1006/jcis.1998.5899>
- 1077 Souza Oliveira, N., Schiavo, J.A., Souza, A.C., Laranjeira,  
1078 L.T., Moraes, E.M.V., Pereira, M.G., 2021. Mineralogy  
1079 and genesis in an alkaline soil system in the southern  
1080 Pantanal wetland, Brazil. South American Earth Sci. J.  
1081 Volume 111, 103456.  
1082 <https://doi.org/10.1016/j.jsames.2021.103456>
- 1083 Taylor, G., Eggleton, R.A., 2017. Silcrete: an Australian  
1084 perspective. Australian Journal of Earth Sciences, 64(8),  
1085 987-1016.  
1086 <https://doi.org/10.1080/08120099.2017.1318167>

- 1087 Theodosoglou, E., et al., 2010. Comparative fourier  
1088 transform infrared and x-ray powder diffraction analysis  
1089 of naturally occurred k-feldspars. Bulletin of the  
1090 Geological Society of Greece, XLIII, No.5, 2752.  
1091 <https://doi.org/10.12681/bgsg.11681>
- 1092 USDA. United States Department of Agriculture. 1987. Soil  
1093 Mechanics Level 1, Module 3, USDA Soil Textural  
1094 Classification Study Guide. USDA Soil Conservation  
1095 Service, Washington DC.
- 1096 Wilson, M.J., 1987. X-ray powder diffraction methods, in:  
1097 Wilson, M.J. (Ed.), A Handbook of Determinative Methods  
1098 in Clay Mineralogy. Chapman and Hall, New York, pp.  
1099 26–98.
- 1100 Vaculíková, L., Plevová, E. 2005. Identification of clay  
1101 minerals and micas in sedimentary rocks. Acta Geodyn.  
1102 Geomater., Vol.2, No.2 (138), 167-175. Available at:  
1103 [https://www.irsm.cas.cz/materialy/acta\\_content/2005\\_02/2](https://www.irsm.cas.cz/materialy/acta_content/2005_02/20_Vaculikova.pdf)  
1104 [0\\_Vaculikova.pdf](https://www.irsm.cas.cz/materialy/acta_content/2005_02/20_Vaculikova.pdf)
- 1105 Vidoca, T. T. 2020. Gênese de argilominerais em solos  
1106 afetados por sais no entorno de lagoas salobras do

- 1107 Pantanal da Nhecolândia. Dissertation. Universidade de  
1108 São Paulo, São Paulo.  
1109 <https://doi.org/10.11606/D.8.2020.tde-23092020-171253>
- 1110 Zhang, Y. G., Ji, J., Balsam, W.L., Liu, L., Chen, J. 2007.  
1111 High resolution hematite and goethite records from ODP  
1112 1143, South China Sea: Co-evolution of monsoonal  
1113 precipitation and El Nino over the past 600,000 years.  
1114 <https://doi.org/10.1016/j.epsl.2007.09.022>
- 1115 Zhou, J., Lau, K.-M. 1998. Does a Monsoon Climate Exist  
1116 over South America? Journal of Climate, 11: 1020-1040.  
1117 [https://doi.org/10.1175/1520-](https://doi.org/10.1175/1520-0442(1998)011<1020:DAMCEO>2.0.CO;2)  
1118 [0442\(1998\)011<1020:DAMCEO>2.0.CO;2](https://doi.org/10.1175/1520-0442(1998)011<1020:DAMCEO>2.0.CO;2)
- 1119 Zviagina, B.B., Drits, V. A., Dorzhieva, O.V. 2020.  
1120 Distinguishing Features and Identification Criteria for K-  
1121 Dioctahedral 1M Micas (Illite-Aluminoceladonite and Illite-  
1122 Glauconite-Celadonite Series) from Middle-Infrared  
1123 Spectroscopy Data. Minerals, 10, 153;  
1124 <https://doi.org/10.3390/min10020153>

1125 **FIGURE CAPTIONS**



1126 Fig. 1. Water dynamics - Main routes of water transfer in an  
1127 alkaline lake according to the literature. (For colour the  
1128 reader is referred to the web version of this article)

1129 Table 1. Saline-alkaline lake data - Parameters used to  
1130 select representative saline-alkaline lakes within the study  
1131 site.

1132 Fig. 2. Location of study - Sites in the Nhecolândia area of  
1133 the Taquari megafan, Pantanal, Brazil. Saline-alkaline  
1134 lakes (1, 4, 6, 7) (B: black, G: green; C: crystalline) and  
1135 freshwater lakes (F). T1 to T7: toposequences associated  
1136 to the studied lakes. Satellite view from Google Earth.  
1137 (For colour the reader is referred to the web version of this  
1138 article)

1139 Fig. 3. Landscape units - Typical vegetation along a saline-  
1140 alkaline lake slope. (For colour the reader is referred to  
1141 the web version of this article).

1142 Fig. 4. Flooding monitoring - Interannual variability of the  
1143 water level in the lakes studied. Satellite views from  
1144 PlanetScope. (For colour the reader is referred to the web  
1145 version of this article).

1146 Fig. 5. Topographic data - Altitude of ridges and lake levels  
1147 measured on the same day. Letters refer to points  
1148 situated on the satellite view. (For colour the reader is  
1149 referred to the web version of this article).

1150 Fig. 6. Apparent electrical conductivity mapping of soils –  
1151 ECS values around each saline-alkaline lake selected,  
1152 with the delimitation of different landscape unit areas and  
1153 the positioning of all boreholes. (For colour the reader is  
1154 referred to the web version of this article).

1155 Fig. 7. Nomenclature of the horizons – Scheme of the  
1156 different color values, matrix hues and textures found in  
1157 the studied soils.

1158 Fig. 8. T1 - Main characteristics of the 1-Black lake  
1159 toposequence. (a) ECS profile; (b) soil horizons, water  
1160 levels, fine fraction and ECW values; c) soil pH. (For  
1161 colour the reader is referred to the web version of this  
1162 article).

1163 Fig. 9. T4 - Main characteristics of the 4-Green lake  
1164 toposequence. (a) ECS profile; (b) soil horizons, water  
1165 levels, fine fraction and ECW values; c) soil pH. (For

1166 colour the reader is referred to the web version of this  
1167 article).

1168 Fig. 10. T6 - Main characteristics of the 6-Black lake  
1169 toposequence. (a) ECS profile; (b) soil horizons, water  
1170 levels, fine fraction and ECW values; c) soil pH. (For  
1171 colour the reader is referred to the web version of this  
1172 article).

1173 Fig. 11. T7 - Main characteristics of the 7-Crystalline lake  
1174 toposequence. (a) ECS profile; (b) soil horizons, water  
1175 levels, fine fraction and ECW values; c) soil pH. (For  
1176 colour the reader is referred to the web version of this  
1177 article).

1178 Fig. 12. Soil mineralogy - Main minerals along the  
1179 sequences. Black points indicate the analyzed samples.  
1180 Unless otherwise stated, the following minerals have been  
1181 identified at each point: quartz, feldspars, micas, kaolinite,  
1182 2:1 expandable clay minerals, goethite, hematite,  
1183 ferrihydrite. The figure therefore represents the absence  
1184 of one or more of these minerals or the presence of

1185 calcite. (For colour the reader is referred to the web  
1186 version of this article).

1187 Fig. 13. Statistical data - PCA correlation circle between  
1188 variables. Percentage on each factorial axis gives the  
1189 explained variance. LOI: loss on ignition.

1190 **SUPPLEMENTARY MATERIAL CAPTION**

1191 File Name:

1192 Manuscript\_ARCS\_Fev\_2023\_Submission\_Supplemental  
1193 File

1194 Caption: Positioning, particle size distribution and pH in  
1195 water of all samples collected for this research.